An Evaluation of ENSO Asymmetry in the Community Climate System Models: A View from the Subsurface

Tao Zhang[1], De-Zheng Sun[1], Richard Neale[2], and Phil Rasch[3]

[1]Cooperative Institute for Research in Environmental Sciences

University of Colorado/NOAA Earth System Research Laboratory

Physical Sciences Division

Boulder, Colorado

[2]National Center for Atmospheric Research, Boulder, Colorado

[3]Pacific Northwest National Laboratory, Richland, Washington

E-mail: tao.zhang@noaa.gov

dezheng.sun@noaa.gov

November 13, 2008

(Submitted to *Journal of Climate*)

Abstract

The asymmetry between El Niño and La Niña is a key aspect of ENSO, and needs to be simulated well by models in order to fully capture the role of ENSO in the climate system. Here we evaluate the asymmetry between the two phases of ENSO in five successive versions of Community Climate System Model (CCSM1, CCSM2, CCSM3 at T42 resolution, CCSM3 at T85 resolution, and the latest CCSM3+NR with Neale and Richter convection scheme). Different from the previous studies, we not only examine the surface signature of ENSO asymmetry, but also its subsurface signature. We attempt to understand the causes of the ENSO asymmetry by comparing the differences among these models as well as the differences between models and the observations.

An underestimate of the ENSO asymmetry is noted in all the models, but the latest version with the Neale and Richter scheme (CCSM3+NR) is getting much closer to the observations than the earlier versions. The net surface heat flux is found to damp the asymmetry in the SST field in both models and observations, but the damping effect in the models is weaker than in observations, thus excluding a role of the surface heat fluxe in contributing to the weaker asymmetry in the SST anomalies associated with ENSO. Examining the subsurface signatures of ENSO—the thermocline depth and the

associated subsurface temperature for the western and eastern Pacific—reveals the same bias—the asymmetry in the models is weaker than in the observations. The weaker asymmetry in the subsurface signatures in the models is related to the lack of asymmetry in the zonal wind stress over the central Pacific which is in turn due to a lack of sufficient asymmetry in deep convection (i.e., the nonlinear dependence of the deep convection on SST). CCSM3+NR has the best simulation of ENSO asymmetry among the five models. It is suggested that the better performance of CCSM3+NR is linked to an enhanced convection over the eastern Pacific during the warm phase of ENSO. An increase of convection over the eastern Pacific during the warm phase leads to an increase in the asymmetry of zonal wind stress and therefore an increase in the asymmetry of subsurface signal, favoring an increase in ENSO asymmetry.

1. Introduction

The El Niño-Southern Oscillation (ENSO) is one of the most important nature modes of the climate system and has been extensively studied (Philander 1990, Sun 2007). Two new dimensions of ENSO have emerged from the more recent investigation—the nonlinear and diabatic aspects of ENSO (Sun 2003, Sun et al. 2004, Sun and Zhang 2006). The sensitivity of ENSO to diabatic heating and its role as a basin-scale heat mixer in the tropical Pacific is linked to a critical quantity of ENSO—the asymmetry between its two phases, or as referred in some other studies, the residual of ENSO (Rodgers et al. 2004; Schopf and Burgman 2006). Relatedly, the ENSO asymmetry is potentially a mechanism for decadal variability (Rodgers et al. 2004; Sun and Yu 2007, submitted to J. Climate), and a cause of the bias in the time-mean background state (Sun and Zhang 2006; Schopf and Burgman 2006).

ENSO asymmetry has long been noted in the SST field—the distribution of the interannual variations of Niño3 SST is found positively skewed (Burgers and Stephenson 1999). They also noted in their study that the early NCAR Climate System Model (CSM1.0; Boville and Gent 1998) underestimates the asymmetry in the distribution of Niño3 SST variations. This bias in NCAR CSM1.0 was noted by later studies that participated in the El Niño Simulation Intercomparison Project (ENSIP)

(Hannachi et al. 2003) and the Coupled Model Intercomparison Project (CMIP) (An et al. 2005). Because NCAR CCSM1 (CSM1.0) severely underestimates the amplitude of ENSO variability, Burgers and Stephenson (1999) suggested a link between the bias in the asymmetry and the bias in the amplitude. The simulation of the amplitude of ENSO variability—measured by the variance of Niño3 SST—in the late versions of NCAR CCSM is greatly improved (Deser et al. 2006). Does the improved simulation of the amplitude of ENSO variability also lead to a better simulation in the asymmetry of ENSO?

To answer this question, and more generally to explore the causes of the ENSO asymmetry, we will evaluate the ENSO asymmetry in five successive versions of the NCAR coupled models—NCAR CSM1 (Boville and Gent 1998), NCAR CCSM2 (Kiehl and Gent 2004), NCAR CCSM3 at T42, NCAR CCSM3 at T85 (Collins et al. 2006a), and NCAR CCSM3+NR (Neale et al. 2007). Recognizing that the El Niño warming and La Niña cooling are driven by the subsurface temperature changes (Zebiak and Cane 1987), we will examine the asymmetry in the subsurface temperature. We will investigate the relationship between SST, convection, wind stress, and surface heat flux, particularly the asymmetry in these fields. By examining the subsurface signal, we reasonably hope that we may obtain more information about the causes of bias in the simulated ENSO in CCSM, particularly in view of the findings by Sun and Zhang (2006) and Sun (2007). In these studies, they found that ENSO has a time mean effect on the vertical temperature structure of the upper ocean—ENSO acts as a vertical heat mixer in the tropical Pacific. This time mean effect is linked to the asymmetry between the upper ocean temperature anomalies during the two phases of ENSO.

This paper is organized as follows. In Section 2, we describe the methodology of our analysis with the basic information about the models. We present the results in Section 3. Summary and discussion are given in Section 4.

2. Methodology, data and model

To quantify the asymmetry of ENSO, we will examine the skewness of interannual variability of SST as well as the subsurface temperature of the equatorial upper Pacific. The skewness, $\sqrt{b_1}$ is defined as $\sqrt{b_1} = m_3/(m_2)^{3/2}$, where m_k is the kth moment, $m_k = (\sum_{i=1}^{N}(X_i - \overline{X})^k)/N$, and where X_i is the ith sample of variable X, $\overline{X}$ is the mean, and N is the number of samples (Burgers and Stephenson 1999). In addition to using skewness to measure the asymmetry of ENSO, we have also done composites of El Niño, and La Niña, and then use the sum of the composite of these two phases of ENSO to measure asymmetry.

Sustained climate modeling work through NCAR and its interaction with the climate community in the US and the world at large has made steady progress in building better and better climate system models. The effort has also created a suite of models with progressive changes, and offered a potential resource to address fundamental climate questions. Up till the writing of this paper, five major versions of NCAR models have been made available to the public. The five NCAR coupled models are NCAR CSM1 (Boville and Gent 1998), NCAR CCSM2 (Kiehl and Gent 2004), NCAR CCSM3 at T42, NCAR CCSM3 at T85 (Collins et al. 2006a), and NCAR CCSM3+NR (Neale et al. 2007). We will examine the ENSO asymmetry in all these five versions and highlight the differences among these models and the progress made in simulating this particular aspect of ENSO.

The atmospheric component of CSM1, CCSM2, CCSM3 at T42, and CCSM3 at T85 is CCM3 (or CAM1) (Kiehl et al., 1998), CAM2 (Kiehl and Gent 2004), CAM3 at T42, and CAM3 at T85 (Collins et al. 2006b; Hack et al. 2006), respectively. From CCM3 (CAM1) to CAM2, there are several changes in physical parameterizations. First, the evaporation of convective precipitation back to the atmosphere was added in order to reduce the dry bias in the free troposphere in the model following Sundqvist (1988). Collins et al. (2002) also updated longwave radiation treatment of water vapor to enhance the longwave cooling in the upper troposphere. In addition, the RK treatment of stratiform clouds (Rasch and Kristjansson, 1998) was modified according to Zhang et al. (2003) that predicts the total (liquid+ice) cloud condensate (Boville et al. 2006; Zhang and Sun 2006). From CAM2 to CAM3, the physics of cloud and precipitation process has been modified extensively by Boville et al. (2006). The modifications include a) separate prognostic treatments of liquid and ice condensate, b) advection, detrainment, and sedimentation of cloud condensate, c) separate treatments of frozen and liquid precipitation, and d) the calculation of the cloud fraction. The radiation code has been updated with new parameterizations for the longwave and shortwave interactions with water vapor (Collins et al. 2006a; Zhang and Sun 2006).

CCM3 (CAM1), CAM2, and CAM3 share the same convection scheme, however. The deep convection is parameterized following Zhang and McFarlane (1995). Shallow convection is parameterized according to Hack (1994).

The ocean component of CSM1 is the NCAR CSM Ocean Model (NCOM) described in Gent et al. (1998). NCOM includes the mesoscale eddy parameterization of Gent and McWilliams (1990), and the vertical mixing scheme based on the *K*-profile parameterization scheme of Large et al. (1994). The ocean component of CCSM2 uses the Parallel Ocean Program code developed at the Los Alamos National Laboratory (Smith et al. 1992). The mesoscale eddy parameterization and the vertical mixing scheme are the same as those used in the ocean component of CSM1. The ocean component of CCSM3 is based upon the Parallel Ocean Program version 1.4.3 (POP; Smith and Gent 2002). The CCSM3 ocean model has two important improvements over CCSM2 as discussed by Danabasoglu et al. (2006). These are modifications to the

Large et al. (1994) *K*-profile parameterization and implementation of spatially varying monthly solar absorption based on ocean color observations.

CCSM3+NR is a developing version based on its immediate predecessor, CCSM3 (Neale et al. 2007). It uses a modified deep convection scheme—Neale and Richter convection scheme to replace the Zhang and McFarlane deep convection scheme (Zhang and McFarlane 1995) used in CCSM3. The changes to the existing parameterization of deep convection (Zhang and McFarlane 1995) are the inclusion of Convective Momentum Transports (CMT) and a dilution approximation for the calculation of Convective Available Potential Energy (CAPE) (Neale et al. 2007).

The observational SST data for our evaluation are from the Hadley Centre Sea Ice and SST (HadISST) dataset (Rayner et al. 2003). The wind stress data are from the National Centers for Environmental Prediction-National Center for Atmospheric Research (NCEP-NCAR) reanalysis (Kalnay et al. 1996) and the surface heat flux data are from the European Centre for Medium-Range Weather Forecasts (ECMWF) reanalyses ERA-40 (Uppala et al., 2005). Observations of precipitation are obtained from the CPC Merged Analysis of Precipitation (CMAP) (Xie and Arkin, 1997). The simple ocean data assimilation (SODA) set (Carton et al. 2000) is used for validating the upper ocean temperature in the models.

3. Results

Figure 1 shows histograms of the distribution of Niño-3 SST anomalies for observations (1950-1999) and five NCAR coupled models. The histogram from the observations has a longer tail on the right. The maximum positive anomaly in the observations is close to 3.5^{o}C while the maximum negative anomaly is limited to -2.5^{o}C. This skewness towards warm El Niño events has been noted by many previous studies (e.g., Burgers and Stephenson 1999 and others). The models, however, clearly have a more Gaussian-like distribution. There are progressive increases in the range of variability from CCSM1 to CCSM3+NR. The range of the variability of Niño-3 SST in the latest version has in fact become very comparable to the observations. The frequency distribution of the anomalies in the latest version is more spread out within the range confined by the maximum positive and negative anomalies, compared to that in four old versions. In other words, there are relatively few instances with weak anomalies in the latest version. The overall distribution for Niño-3 anomalies is much closer to normal distribution in the NCAR models than in observations. A positive skewness is evident in the histogram for the latest version, however.

Table 1 lists the skewness of Niño-3 SST anomalies from observations and the models together with their variance. The numbers in the table confirm the impression from the histograms that the models underestimate the skewness of Niño-3 SST anomalies. Among the five models, the latest CCSM3+NR has the strongest ENSO variability and a significant positive skewness. It is interesting to note that there is a much weaker ENSO variability in CCSM1, but the skewness in CCSM1 is comparable to that in CCSM3+NR. An et al. (2005) has pointed out that the small standard deviation may cause the large skewness according to the definition of skewness. More importantly, one see from Table 1 that increases in the variance of Niño-3 SST anomalies does not necessarily leads to an increase in the skewness. For example, measured by the variance of Niño-3 SST anomalies alone, one would conclude that the level of ENSO variability in CCSM2, CCSM3, and CCSM3 at T85 is comparable to observations, but quantifying the skewness of Niño-3 SST anomalies indicates otherwise.

Another measure of ENSO asymmetry is to construct composites of El Niño and La Niña events. Figure 2 gives the spatial pattern of composite SST anomalies during El Niño and La Niña events from observations and five NCAR models. Both the El Niño and La Niña composites in observations have a wider meridional extension of the SST anomalies than in four earlier versions of NCAR models (CCSM1, CCSM2, and two CCSM3 models). Positive SST anomalies associated with El Niño and negative SST anomalies associated with La Niña in these models also extend too far westward, consistent with the existence of an excessive cold-tongue in these models (Sun et al. 2006). The latest CCSM3+NR has an improvement in the zonal and meridional extension of the SST anomalies and this has been noted already by Neale et al. (2007). The observed maximum SST anomaly of 1.6 ^{o}C around 110^{o}W is well captured in

CCSM3+NR during the warm phase, while the negative SST anomaly is somewhat overestimated in the model during the cold phase. The spatial distribution of the asymmetry between El Niño and La Niña events is shown in Figure 3. The asymmetry pattern is defined as the sum of El Niño and La Niña composites. In observations, the asymmetry map has a similar spatial structure of the El Nino event (Fig. 3 a). The figure is characterized by positive SST anomalies of about 0.2-0.5^{o}C over the central and eastern tropical Pacific and small negative anomalies of about -0.1^{o}C over the western tropical Pacific. The main bias in the models is a severe underestimate of positive anomalies over the eastern tropical Pacific, indicating a weak asymmetry in the NCAR coupled models (Figure 3b-3f). The skewness pattern (contour of right panel) is very similar to the pattern of sum of warm and cold events (left panel) and indicates again an underestimate of positive skewness over the eastern tropical Pacific in the models. By comparison, the latest CCSM3+NR stands out as the one resembling the observations most, although it has a weaker positive skewness in the eastern Pacific and a stronger negative skewness in the western Pacific. We have also noted that over the western Pacific, the cold bias in SST climatology (shaded) is accompanied with a positive skewness opposite to the observed (Figures 3h, 3i) and the warm bias in SST climatology (shaded) is accompanied with a stronger negative skewness (Figures 3j, 3l). This is probably due to the sensitivity of deep convection to the total SST, a point we will return later.

The precipitation anomalies during the warm and cold phases are shown in Figure 4. Observations show that the maximum of precipitation anomalies during the warm phase locates at about 180^o with the magnitude of 4 mm day^{-1} whereas the maximum of precipitation anomalies during the cold phase shifts westwards and centers at 170^{o}E with the magnitude of -3 mm day^{-1}. The lack of convection during the warm phase over the equatorial central and eastern Pacific is evident in four old versions, but one can see the progressive improvement in these models in the location of the center of response as well as the magnitude of the response. The center of maximum precipitation in CCSM3+NR is even more eastward than in the observations. Clearly, the precipitation anomalies during the warm phase of ENSO over the eastern Pacific in this latest version are very comparable to that in the observations. Interestingly, the maximum precipitation response in this new model is still somewhat weaker than the observations. The CCSM3+NR also starts to get the negative anomalies in the western Pacific, a feature that is almost entirely missing in four old versions in the western Pacific.

The negative precipitation anomalies during the cold phase in the models (CCSM1, CCSM2, and CCSM3 at T42) are generally weaker than in the observations in the central and eastern Pacific. In the central Pacific, the negative precipitation anomalies in CCSM3+NR are comparable to the observations. The precipitation anomaly in the far eastern Pacific in this latest version is even stronger than in the observations, consistent with the stronger negative SST anomalies over that region (Fig.2l). A common bias in all these models is the lack of the positive precipitation anomalies in the western Pacific.

The associated zonal wind stress anomalies during the warm and cold phases are shown in Figure 5. During the warm phase the positive zonal wind stress anomalies are more confined within 5^oS-5^oN and the magnitude is underestimated in four old versions. But the progressive improvement is again evident. In contrast to the four earlier versions, CCSM3+NR is distinctly closer to the observations. It not only has an improvement in simulating the meridional extension of zonal wind stress anomalies, but also has an improvement in simulating the magnitude of zonal wind stress anomalies. The new model also gets the correct location of maximum wind stress anomaly around 150^oW in the warm phase while other models has this location more westward by 10^o (left panel of Fig.5). During the cold phase the negative anomalies of zonal wind stress are still confined to the equatorial region of 5^oS-5^oN in the old models and the magnitude is too weak in CCSM1 and CCSM2. CCSM3+NR better captures the pattern of negative anomalies (right panel of Fig.5). We also note that the maximum negative wind stress anomalies are located in the region of 150^oW-130^oW in NCEP data (Fig.5g), but they are extended from 170^oE to 140^oW in CCSM3+NR (Fig.5l), associated with a wider zonal distribution of negative precipitation anomalies during the cold phase (Fig.4l). The stronger negative zonal wind stress anomaly in CCSM3+NR is also consistent with a stronger negative SST anomaly during the cold phase (Fig.2l).

The sum between warm composite anomalies and cold composite anomalies in precipitation and zonal wind stress is shown in Figure 6. Observations show a strong asymmetry in precipitation fields—the positive anomalies during the warm phase are larger than the negative anomalies during the cold phase in the central and eastern Pacific, and the negative anomalies during the warm phase are also larger than the positive anomalies during the cold phase in the western Pacific (Figure 6a). With the exception of the CCSM3+NR, such an asymmetry does not exist in the models. The underestimate of the asymmetry in the precipitation anomalies in four old versions (Figures 6b-6e) is due to the lack of convection in the warm phase (Figures 4b-4e). An increase of precipitation in the warm phase over the central and eastern Pacific in the latest CCSM3+NR improves the asymmetry of precipitation (Figure 6f). In response to the weak asymmetry in precipitation anomalies, the asymmetry in zonal wind stress anomalies is also weak in the NCAR models (right panel of Figure 6). Again, the new version CCSM3+NR has an improved asymmetry pattern of zonal wind stress anomalies because of the improvement in simulating the asymmetry in the precipitation anomalies (Figures 6f and 6l). A close look of Figure 6j and Figure 6k reveals that there is a slight negative asymmetry of zonal wind stress in two CCSM3 models over the central Pacific, contrary to the observed, which may contribute to the negative SST asymmetry in that region (Figures 3d and 3e).

Figure 7 shows the composite of the net surface heat fluxes for the two phases of

ENSO. The figures show that four earlier versions of the NCAR model underestimate the negative heat flux anomalies during the warm phase. These models also underestimate the positive anomalies during the cold phase. Regression of the surface heat flux onto the SST further reveals that the four earlier versions of the model underestimate the damping effect of the net surface heat flux on the local SST—the slope of the surface heat flux against the SST in these models is much weaker than that in the observations (Figure 8). The surface heat flux-SST relationship is much improved in CCSM3+NR (-18.4 $Wm^{-2}K^{-1}$ in the model versus the observed -21.5 $Wm^{-2}K^{-1}$. Consistent with the improvement in asymmetry of convection (Figure 6f), the new model also has an improved asymmetry pattern in the surface heat flux although the magnitude of asymmetry is underestimated over the central and eastern Pacific (by 10~15 Wm^{-2}) (Figure 8l). The match of the stronger positive asymmetry of heat flux over the western Pacific (Figure 8l) with the stronger negative asymmetry of SST over that region (Figures 3f and 3l) indicates a good negative correlation between the asymmetry of surface heat flux and the asymmetry of SST in the new model. It is clear that all the NCAR models underestimate the damping effect of surface heat flux on SST over the central and eastern Pacific (right panel of Fig.8). Thus the underestimate of the ENSO asymmetry is not likely due to the contribution from the surface heat flux.

Next we will look at the asymmetry of subsurface signal. As demonstrated in the pioneering studies of ENSO (Zebiak and Cane 1987 and others), the SST anomaly in the eastern Pacific associated ENSO is driven by the subsurface temperature anomaly in that region which is in turn related to the subsurface temperature anomaly in the western Pacific. Figure 9 shows the equatorial upper ocean temperature anomalies during both phases of ENSO. Observations show a maximum positive anomaly of 2.5 ^{o}C during warm phase in the eastern Pacific (Fig.9a) and a maximum negative anomaly of -1.5^{o}C during cold phase in the eastern Pacific (Fig.9g). The location of the maximum response occurs approximately in the region of 120^{o}W to the eastern coast at a depth about 50-100 m. During the warm phase, four old versions of CCSM have a much weaker positive subsurface temperature anomaly over the eastern Pacific. The underestimate of the anomaly ranges from about 2 ^{o}C in CCSM1 to 1 ^{o}C in CCSM3. The positive anomalies in the models are more confined to the surface and extend too far to the west. The accompanying negative temperature anomalies in the subsurface of the western Pacific are also underestimated in these models. The maximum negative temperature anomaly occurs at about the same depth as that in the observations, but is more eastward. The axis of maximum negative temperature anomaly in the depth-longitude plane is more horizontal in the models than in the observations. In terms of magnitude, the upper ocean temperature anomalies in the latest version CCSM3+NR is comparable to those in observations.

During the cold phase, the models do a better job in simulating the upper ocean temperature anomalies than in the warm phase. The negative temperature anomalies in

CCSM1 and CCSM2 are underestimated, but those in two versions of CCSM3 are comparable to the observed over the eastern Pacific. The latest version CCSM3+NR has stronger subsurface temperature anomalies than in the observations. CCSM3+NR differs from the observed value in its simulation of the subsurface temperature anomaly over the western Pacific by as much as 0.25 ^{o}C. Again, we noted that over the western Pacific the shape of subsurface temperature anomalies in observations differs from those in the models—the former have a more downward tile while the latter are more horizontal.

Fig. 10 shows the time-mean thermocline depth (indicated by 20 ^{o}C isotherm depth) in observations and models. The observed thermocline depth over the western Pacific increases from 150 m to around 175 m, showing a downward tilt. The modeled thermocline depth is either flat or has slightly upward tilt in the western Pacific. In terms of zonal extent, there is a progressive increase in the size of the western Pacific warm-pool.

Figure 11 shows a basin-wide view of the thermocline depth anomalies during the warm and cold phases. All the models except CCSM1 can simulate the observed feature: thermocline depth is increased in the tropical eastern Pacific and decreased in the central and western Pacific during the warm phase, and a reversed situation occurs during the cold phase. The magnitude of the thermocline depth anomalies, however, is underestimated in the models especially over the eastern Pacific during the warm phase. This may contribute to the small subsurface temperature anomalies in most models during the warm phase. By comparison, CCSM3+NR has a close pattern to the observed because of an improvement in the meridional extension, which may be due to a better simulation in the wind stress anomaly (Figures 5f and 5l).

To examine the subsurface signatures of ENSO asymmetry, we add the upper ocean temperature anomalies over the two phases. We do the same sum for the depth of thermocline. Figure 12 shows the results—the left panels show the asymmetry in the upper ocean temperature anomalies and the right panels show the asymmetry in the thermocline depth anomalies. Observations indicate a positive asymmetry of subsurface temperature of 1 ^{o}C around 75-m depth over the eastern Pacific, and a negative asymmetry of 0.4 ^{o}C in subsurface temperature in the western Pacific. All the models underestimate the asymmetry in subsurface temperature. Therefore the weaker SST asymmetry in the models is likely due to an underestimate of the asymmetry in subsurface temperature. Again, CCSM3+NR has an increased positive asymmetry in subsurface temperature compared to other old versions (Fig.12f). The underestimate of the asymmetry in the subsurface temperature anomalies also shows up in the asymmetry in the depth of thermocline (right panel of Fig.12). The asymmetry in the observed thermocline depth anomalies is characterized by a broad negative region in the western Pacific. This feature is largely absent in the four earlier versions of the model. The latest version of the model has a negative asymmetry in the western Pacific, but the negative asymmetry is still too confined to the equator, and the maximum is located too far to the east.

Fig. 13 further shows the meridional structures of the asymmetry in the upper ocean temperature anomalies over the western Pacific and eastern Pacific. Observations are characterized by two maximum values of negative asymmetry off the equator in both hemispheres over the western Pacific (Fig.13a) and a strong positive asymmetry right at the equator over the eastern Pacific (Fig.13g). The negative asymmetry over the western Pacific covers a wider meridional region extending from 10 ^{o}S to 10 ^{o}N while the positive asymmetry over the eastern Pacific is mainly confined within the equator (5 ^{o}S-5 ^{o}N). Except for a better simulation of the negative asymmetry over the region of 5 ^{o}N-10 ^{o}N in the western Pacific in CCSM3 (Fig.13d), all the models underestimate the negative asymmetry over the western Pacific and the positive asymmetry over the eastern Pacific. The improvement of the asymmetry in the meridional sections over the eastern Pacific in the new version CCSM3+NR is not as obvious as that in the zonal cross sections noted earlier (Fig.13l). This is expected because of the cancellation between the positive asymmetry over the far eastern Pacific and the overly negative asymmetry over the region of 150 ^{o}W-120 ^{o}W as shown in Fig.12f.

To obtain a qualitative measure of the asymmetry in the subsurface temperature, we plot the histogram of the monthly mean Niño-3 subsurface temperature anomalies (Figure 14). The figure shows that the observed Niño-3 subsurface temperature anomalies are skewed to the positive values and the maximum positive anomalies can reach more than 6 ^{o}C. The underestimate of the maximum positive anomalies in the models ranges from 5 ^{o}C in CCSM1 to 2 ^{o}C in CCSM3+NR. Although the overall distribution in the models is close to normal distribution, the new version CCSM3+NR has a more similar shape to the observed among five models.

The skewness and variance of the subsurface temperature anomalies are further shown in Table 2. The results confirm that all the models underestimate the variability and skewness of Niño-3 subsurface temperature. Comparing Table 2 with Table 1 indicates that the interannual variability of Niño-3 subsurface temperature is almost as twice strong as that of Niño-3 SST in observations. But the contrast in the strength of variability between the surface and the subsurface in the models is not as significant as the observed. In fact, the subsurface temperature variability is even weaker than SST variability in two old versions (CCSM1 and CCSM2). Table 2 also shows that in the models, there are a good correspondence between the weaker variability of subsurface temperature and the underestimate of the skewness of subsurface temperature. From Table 2, we find that over the western Pacific the observed negative asymmetry of subsurface temperature (Tsub_WP) is underestimated in all the models, which is consistent with the results shown in the left panel of Figure 12. Further considering the underestimate of the positive asymmetry in Niño-3 subsurface temperature (Tsub_Nino3), we are not surprised at the findings that the underestimate of the positive asymmetry in the difference of subsurface temperature between Niño-3 region and western Pacific (Tsub_diff) is more severe in all the models, accompanied with an enhanced underestimate of the variability of subsurface temperature in most models (the underestimate of Tsub_diff variability in CCSM3+NR is not as much as that of Tsub_Nino3 variability due to an increase of Tsub_WP variability in this model). Stronger SST variability does not necessarily result in a stronger skewness. For example, we note that CCSM2 and CCSM3+NR have a larger SST variability than observations but have a weaker skewness of SST. CCSM1 has a much weaker SST variability than CCSM2 but the skewness value in the former is much larger than that in the latter (Table 1). A good match of the temperature variability with the temperature skewness is evident in the subsurface (Table 2). It is thus suggested that the subsurface temperature anomalies may be a good proxy as a measure of the relationship between ENSO variability and asymmetry. Clearly, the present findings reveal that the lack of the asymmetry in SST field in the NCAR models is linked to an underestimate of the asymmetry in subsurface temperature.

4. Summary

In this study, we have evaluated the ENSO asymmetry in five successive versions of Community Climate System Models (CCSMs). We find that all the versions underestimate the ENSO asymmetry. This underestimate is found in both the SST and the subsurface temperature signatures of ENSO. We also find that the net surface heat flux damps the ENSO asymmetry in the SST field and the models underestimate this damping effect. We suggest that the lack of asymmetry in the SST field of ENSO is due to the weak thermocline depth asymmetry in the models. The latter may be due to the lack of asymmetry in zonal wind stress over the central Pacific caused by a weaker nonlinear relationship between deep convection and SST in the central and eastern Pacific.

Because of the nonlinear dependence of deep convection on the SST, the zonal winds respond asymmetrically to SST anomalies. In the western Pacific warm pool region, small SST anomalies can excite large precipitation anomalies whereas positive SST anomalies of appreciable magnitude are needed to induce convection in the cold eastern equatorial Pacific. One the other hand, negative SST anomalies in the cold eastern equatorial Pacific have no further effect on regions that are normally dry (Hoerling et al. 1997). Therefore the wind response to SST anomaly pattern of El Niño is different from the wind response to the anomalous SST pattern associated with La Niña (Hoerling et al. 1997; Kang and Kug 2002). We suggest that the asymmetric response of the zonal winds to SST anomalies could be an important cause of the ENSO asymmetry. The asymmetry in zonal wind stress results in an asymmetry in the subsurface temperature response. All the five models have a weak asymmetry in the zonal wind stress and therefore a weak asymmetry in the subsurface signatures. The weaker asymmetry in the subsurface is then reflected in the SST field. Test of this hypothesis will be described in a separate paper.

The evaluation also reveals that models with stronger variance in the Niño-3 SST can have smaller SST skewness. Therefore, the level of ENSO activity cannot be measured adequately by Niño-3 SST variance alone. In the subsurface, we note a good correspondence between the level of variance of the temperature and skewness of temperature. The results underscore the use of the subsurface temperature variability in measuring the level of ENSO activity.

Among five NCAR models, the latest CCSM3+NR has the best simulation of the ENSO asymmetry. Apparently, the replacement of Zhang and McFarlane deep convection scheme (Zhang and McFarlane 1995) by the Neale and Richter convection scheme (Neale et al. 2007) in the latest CCSM3+NR results in an increase in deep convection over the eastern Pacific during the warm phase, and the enhanced deep convection increases the asymmetry in the zonal wind stress response to SST anomalies. The increased asymmetry in zonal wind stress over the central Pacific leads to an enhancement in the asymmetry of thermocline depth over the coastal regions of eastern Pacific, where the associated subsurface temperature asymmetry is increased. The enhanced asymmetry of subsurface temperature then results in an improvement of ENSO asymmetry in the new model in the SST field through the upwelling.

The ENSO asymmetry over the eastern Pacific in CCSM3+NR is still weaker than that in observations. The reason appears to be that the asymmetry of convection is still somewhat weaker in the new model due to the overestimate of the negative precipitation anomaly over the eastern Pacific during the cold phase. Interestingly, we find that over the western Pacific a cold bias in SST climatology is accompanied with a positive skewness opposite to the observed and a warm bias in SST climatology is accompanied with a stronger negative skewness. This indicates that the dependence of deep convection on the total SST plays a role in determining the skewness in SST, particularly in regions with weak upwelling.

Acknowledgement

This research was supported by NOAA's Climate Dynamics and Environmental Prediction Program, and by NSF's climate dynamics program under ATM-9912434, ATM-0332760, and ATM 0553111.

Table captions

Table 1. Statistics estimated for monthly time series of Niño-3 SST anomalies from observations and five NCAR coupled models. The length of data for computing the statistics is 50 years for all the models and observations (1950–99). The values listed in parentheses are the results from 100-year-long model data and observations (1900-1999).

Table 2. Statistics estimated for monthly time series of equatorial subsurface temperature anomalies from SODA data and five NCAR coupled models. The subsurface temperature anomalies at 75-m depth over the Niño-3 (210°–270°E, 5°S–5°N) region (Tsub_Nino3), at 150-m depth over the western Pacific (130°–170°E, 5°S–5°N) (Tsub_WP), and from the difference between them (Tsub_diff) are used in the calculation. The length of data for computing the statistics is 50 years for all the five models and SODA data (1950–99).

Figure captions

Figure 1. Histograms of the monthly mean Niño-3 SST anomalies from observations and five NCAR coupled models. The normal distributions with the respective standard deviation are plotted as dashed line. A bin width of 0.2°C is used. The length of data used in the calculation is 50 years for all the models and observations (1950–99).

Figure 2. Spatial distributions of composite SST anomalies during El Niño (left panel) and La Niña (right panel) events from observations and five NCAR coupled models. The positive (negative) anomalies of Niño-3 SST with a value greater than 0.5°C (-0.5°C) are selected to construct composites of warm (cold) events. The length of data used in the calculation is 50 years for all the NCAR models and observations (1950–99).

Figure 3. Spatial distributions of the asymmetry between El Niño and La Niña events from observations and five NCAR coupled models. The left panel is the sum of of El Niño and La Niña composite SST anomalies, and the right panel is the skewness pattern of SST anomalies (contour) overlaid with the difference in SST climatology between

models and observations (shaded). The positive (negative) anomalies of Niño-3 SST with a value greater than 0.5^{o}C (-0.5^{o}C) are selected to construct composites of warm (cold) events. The length of data used in the calculation is 50 years for all the models and observations (1950–99).

Figure 4. Spatial distributions of precipitation anomalies during warm periods (left panel) and cold periods (right panel). The length of data used in the calculation is 50 years for all the NCAR models and 28 years for the CMAP precipitation (1979-2006).

Figure 5. Spatial distributions of zonal wind stress anomalies during warm periods (left panel) and cold periods (right panel). The length of data used in the calculation is 50 years for all the NCAR models and NCEP zonal wind stress (1950-1999).

Figure 6. Spatial distributions of asymmetry in precipitation (left panel) and in zonal wind stress (right panel). Shown are the results from the sum between warm anomalies and cold anomalies. The length of data used in the calculation is 50 years for all the models and NCEP zonal wind stress (1950-1999), and 28 years for the CMAP precipitation (1979-2006).

Figure 7. Spatial distributions of net surface heat flux anomalies during warm periods (left panel) and cold periods (right panel). The length of data used in the calculation is 50 years for all the NCAR models and 45 years for the ERA-40 (September 1957-August 2002).

Figure 8. Scatter plot between the net surface heat flux anomalies and the SST anomalies over the Niño-3 region (left panel) and the spatial distributions of asymmetry in net surface heat flux (right panel). The asymmetry in net surface heat flux is defined as the sum between warm anomalies and cold anomalies. The length of data used in the calculation is 50 years for all the models and 45 years for the ERA-40 (September 1957-August 2002).

Figure 9. The composite anomalies of equatorial (5^oS-5^oN) upper ocean temperature during warm periods (left panel) and cold periods (right panel). The length of data used in the calculation is 50 years for all the five models and SODA data (1950–99).

Figure 10. Time-mean equatorial (5^oS-5^oN) upper ocean temperature from five models

and SODA data. The 20 °C isotherm is plotted as red solid line in the figure. The length of data used in the calculation is 50 years for all the five models and SODA data (1950–99).

Figure 11. Spatial distributions of 20 °C isotherm depth anomalies during warm periods (left panel) and cold periods (right panel). The length of data used in the calculation is 50 years for all the five models and SODA data (1950-1999).

Figure 12. The asymmetry in the equatorial upper ocean temperature (left panel) and in 20 °C isotherm depth (right panel). Shown are the results from the sum between warm anomalies and cold anomalies. The length of data used in the calculation is 50 years for all the five models and SODA data (1950-1999).

Figure 13. The asymmetry in meridional cross sections of the upper ocean temperature over the western Pacific (130°–170°E) (left panel) and Niño-3 region (210°–270°E) (right panel). Shown are the results from the sum between warm anomalies and cold anomalies. The length of data used in the calculation is 50 years for all the five models and SODA data (1950-1999).

Figure 14. Histograms of the monthly mean Niño-3 subsurface temperature anomalies at 75-m depth. The normal distributions with the respective standard deviation are plotted as dashed line. A bin width of 0.2^{o}C is used. The length of data used in the calculation is 50 years for all the models and SODA data (1950–99).

References

An, S.-I., Y.-G. Ham, J.-S. Kug, F.-F. Jin, and I.-S. Kang, 2005: El Niño–La Niña Asymmetry in the Coupled Model Intercomparison Project Simulations. *J. Climate*, **18**, 2617–2627.

Boville B. A., and P. R. Gent, 1998: The NCAR Climate System Model, version one. *J. Climate*, **11**, 1115–1130.

Boville, B. A., P. J. Rasch, J. J. Hack, and J. R. McCaa, 2006: Representation of clouds and precipitation processes in the Community Atmosphere Model (CAM3). *J. Climate*, **19**, 2184–2198.

Burgers G., and D. B. Stephenson, 1999: The "normality" of El Nino. *Geophys. Res. Lett.*, **26**, 1027–1030.

Carton J., G. Chepurin, X. Cao, and B. Giese, 2000: A simple ocean data assimilation analysis of the global upper ocean 1950–95. Part I: Methodology. *J. Phys. Oceanogr,* 30, 294–309.

Collins, W. D., J. K. Hackney, and D. P. Edwards, 2002: An updated parameterization for infrared emission and absorption by water vapor in the National Center for Atmospheric Research Community Atmosphere Model. *J. Geophys. Res.,* 107(D22), 4664, doi:10.1029/2001JD001365.

Collins W. D., Coauthors, 2006a: The Community Climate System Model version 3

(CCSM3). *J. Climate*, **19**, 2122–2143.

Collins, W. D., P. J. Rasch, B. A. Boville, J. J. Hack, J. R. McCaa, D. L. Williamson, B. P. Briegleb, C. M. Bitz, S.-J. Lin, and M. H. Zhang, 2006b: The formulation and atmospheric simulation of the Community Atmosphere Model version 3 (CAM3), *J. Climate*, **19**, 2144–2161.

Danabasoglu G., W. G. Large, J. J. Tribbia, P. R. Gent, B. P. Briegleb, and J. C. McWilliams, 2006: Diurnal coupling in the tropical oceans of CCSM3. *J. Climate*, **19**, 2347–2365.

Deser, C., A. Capotondi, R. Saravanan, and A. S. Phillips, 2006: Tropical Pacific and Atlantic Climate Variability in CCSM3. *J. Climate*, **19,** 2451–2481.

Gent, P. R., F. O. Bryan, G. Danabasoglu, S. C. Doney, W. R. Holland, W. G. Large, and J. C. McWilliams, 1998: The NCAR Climate System Model global ocean component. *J. Climate*, **11**, 1287–1306.

Gent, P. R., and J. C. McWilliams, 1990: Isopycnal mixing in ocean circulation models. *J. Phys. Oceanogr.,* **20**, 150–155.

Hack, J. J., 1994: Parameterization of moist convection in the National Center for Atmospheric Research Community Climate Model (CCM2). *J. Geophys. Res.,* **99**, 5551–5568.

Hack, J. J., J. M. Caron, G. Danabasoglu, K. W. Oleson, C. M. Bitz, and J. E. Truesdale, 2006: CCSM-CAM3 climate simulation sensitivity to changes in horizontal resolution. *J. Climate*, **19**, 2267–2289.

Hannachi A., D. Stephenson, and K. Sperber, 2003: Probablity-based methods for quantifying nonlineararity in the ENSO. *Climate Dyn.*, **20**, 241–256.

Hoerling, M. P., A. Kumar, and M. Zhong, 1997: El Niño, La Niña, and the nonlinearity of their teleconnections. J. Climate, **10**, 1769–1786**.**

Kalnay, E., et al., 1996: The NCEP/NCAR 40-year reanalysis project, Bull. Am. Meteorol. Soc., 77, 437–471.

Kang I.-S., and J.-S. Kug, 2002: El Niño and La Niña sea surface temperature anomalies: Asymmetry characteristics associated with their wind stress anomalies. *J. Geophys. Res.*, **107**, 4372, doi:10.1029/2001JD000393.

Kiehl, J. T., J. J. Hack, G. Bonan, B. A. Boville, D. Williamson, and P. J. Rasch, 1998, The National Center for Atmospheric Research Community Climate Model: CCM3, *J. Climate*, **11**, 1131–1149.

Kiehl J., and P. Gent, 2004: The Community Climate System Model, version 2. *J. Climate*, **17**, 3666–3682.

Large W. G., J. C. McWilliams, and S. C. Doney, 1994: Oceanic vertical mixing: A review and a model with a nonlocal boundary layer parameterization. *Rev. Geophys,* **32**, 363–403.

Neale R. B., J. H. Richter, and M. Jochum, 2007: The impact of convection on ENSO: From a delayed oscillator to a series of events. *J. Climate*, (Submitted).

Philander S. G., 1990: *El Niño, La Niña, and the Southern Oscillation*. Academic Press, 289 pp.

Rasch, P. J., and J. E. Kristjansson, 1998: A comparison of the CCM3 model climate using diagnosed and predicted condensate parameterizations. *J. Climate*, **11**, 1587–1614.

Rayner N. A., D. E. Parker, E. B. Horton, C. K. Folland, L. V. Alexander, D. P. Rowell, E. C. Kent, and A. Kaplan, 2003: Global analyses of sea surface temperature, sea ice and night marine air temperature since the late nineteenth century. *J. Geophys. Res.*, **108**, 4407, doi:10.1029/2002JD002670.

Rodgers, K. B., P. Friederichs, and M. Latif, 2004: Tropical Pacific decadal variability and its relation to decadal modulation of ENSO. *J. Climate*, **17**, 3761–3774.

Schopf, P. S., and R. J. Burgman, 2006: A simple mechanism for ENSO residuals and asymmetry. *J. Climate*, **19**, 3167–3179.

Smith R. D., J. K. Dukowicz, and R. C. Malone, 1992: Parallel ocean general circulation modeling. *Physica D*, **60**, 38–61.

Smith R. D., and P. R. Gent, 2002: Reference manual for the Parallel Ocean Program (POP), ocean component of the Community Climate System Model (CCSM2.0 and 3.0). Los Alamos National Laboratory Tech. Rep. LA-UR-02-2484, 75 pp. [Available online at http://www.ccsm.ucar.edu/models/ccsm3.0/pop.].

Sun, D.-Z., 2003: A possible effect of an increase in the warm-pool SST on the magnitude of El Niño warming. *J. Climate*, **16**, 185-205.

Sun, D.-Z., T. Zhang, and S.-I. Shin, 2004: The effect of subtropical cooling on the amplitude of ENSO: a numerical study. *J. Climate* , **17**, 3786-3798.

Sun, D.-Z., and T. Zhang, 2006: A Regulatory Effect of ENSO on the Time-Mean Thermal Stratification of the Equatorial Upper Ocean. *Geophys. Res. Lett.*, 33, L07710, doi:10.1029/2005GL025296.

Sun, D.-Z., 2007: The Role of ENSO in Regulating its Background State. In "Nonlinear Dynamics in Geosciences", pages 537-555, Springer New York, 604 pages, Edited by J. Elsner and A. Tsonis.

Sun, D.-Z., T. Zhang, C. Covey, S. A. Klein, W. D. Collins, J. J. Hack, J. T. Kiehl, G. A. Meehl, I. M. Held, and M. Suarez, 2006: Radiative and Dynamical Feedbacks Over the Equatorial Cold-tongue: Results from Nine Atmospheric GCMs. *J. Climate*, **19**, 4059-4074.

Sun, F., and J.-Y. Yu, 2007: A 10-15year Modulation Cycle of ENSO Intensity. *J. Climate*, (Submitted).

Sundqvist H., 1988: Parameterization of condensation and associated clouds in models for weather prediction and general circulation simulation. Physically-based Modeling and Simulation of Climate and Climate Change, Vol. 1, M. E. Schlesinger, Ed., Kluwer Academic, 433–461.

Trenberth K. E., 1997: The definition of El Niño, *Bull. Am. Meteorol. Soc.,* **78**, 2771-2777.

Uppala, S. M., et al., 2005: The ERA-40 reanalysis, Q. J. R. Meteorol. Soc., 131, 2961–3012, doi:10.1256/qj.04.176/.

Xie, P., and P. A. Arkin, 1997: Global precipitation: A 17-year monthly analysis based on gauge observations, satellite estimates, and numerical model outputs, Bull. Am. Meteorol. Soc., 78, 2539–2558.

Zebiak, S. E., and M. A. Cane, 1987: A model El Niño–Southern Oscillation. *Mon. Wea. Rev*, **115**, 2262–2278.

Zhang, G. J., and N. A. McFarlane, 1995: Sensitivity of climate simulations to the parameterization of cumulus convection in the Canadian Climate Centre general circulation model, Atmos. Ocean, 33, 407–446.

Zhang M., W. Lin, C. S. Bretherton, J. J. Hack, and P. J. Rasch, 2003: A modified formulation of fractional stratiform condensation rate in the NCAR Community Atmospheric Model (CAM2). J. Geophys. Res, 108, 4035, doi:10.1029/2002JD002523.

Zhang, T., and D.-Z. Sun, 2006: Response of water vapor and clouds to El Niño warming in three National Center for Atmospheric Research atmospheric models, J. Geophys. Res., 111, D17103, doi:10.1029/2005JD006700.

Table 1. Statistics estimated for monthly Niño-3 time series from observations and five NCAR coupled models. The length of data for computing the statistics is 50 years for all the models and observations (1950–99). The values listed in parentheses are the results from 100-year-long model data and observations (1900-1999).

Source	standard deviation	skewness
Observed	0.88 ^oC (0.82)	0.86 (0.62)
CCSM1	0.47 ^oC (0.47)	0.36 (0.31)
CCSM2	0.92 ^oC (0.92)	0.012 (0.052)
CCSM3	0.81 ^oC (0.84)	0.089 (-0.10)
CCSM3(T85)	0.79 ^oC (0.85)	-0.13 (-0.20)
CCSM3+NR	1.03 ^oC (1.12)	0.31 (0.17)

Table 2. Statistics estimated for monthly time series of equatorial subsurface temperature anomalies from SODA data and five NCAR coupled models. The subsurface temperature anomalies at 75-m depth over the Niño-3 (210°–270°E, 5°S–5°N) region (Tsub_Nino3), at 150-m depth over the western Pacific (130°–170°E, 5°S–5°N) (Tsub_WP), and from the difference between them (Tsub_diff) are used in the calculation. The length of data for computing the statistics is 50 years for all the five models and SODA data (1950–99).

Source	standard deviation (^{o}C)			skewness		
	Tsub_WP	Tsub_Nino3	Tsub_diff	Tsub_WP	Tsub_Nino3	Tsub_diff
Observed	1.36	1.51	2.44	-0.18	0.45	0.61
CCSM1	0.36	0.37	0.53	0.038	0.063	-0.065
CCSM2	1.21	0.77	1.53	0.016	0.15	0.089
CCSM3	1.10	1.00	1.66	0.092	0.23	-0.22
CCSM3(T85)	1.08	0.81	1.54	0.10	0.21	0.010
CCSM3+NR	1.42	1.36	2.36	0.22	0.24	0.11

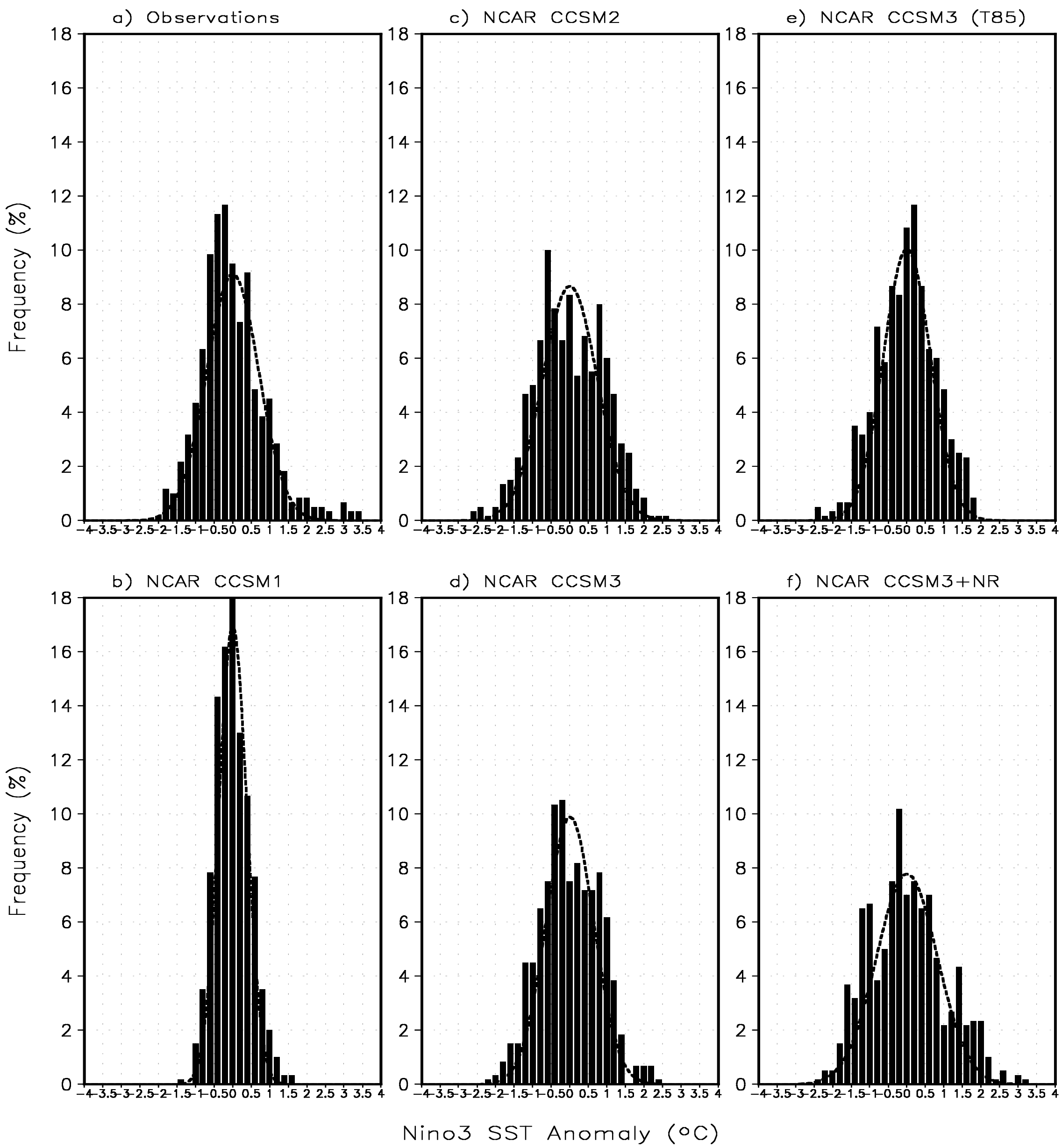

Figure 1. Histograms of the monthly mean Niño-3 SST anomalies from observations and five NCAR coupled models. The normal distributions with the respective standard deviation are plotted as dashed line. A bin width of 0.2°C is used. The length of data used in the calculation is 50 years for all the models and observations (1950–99).

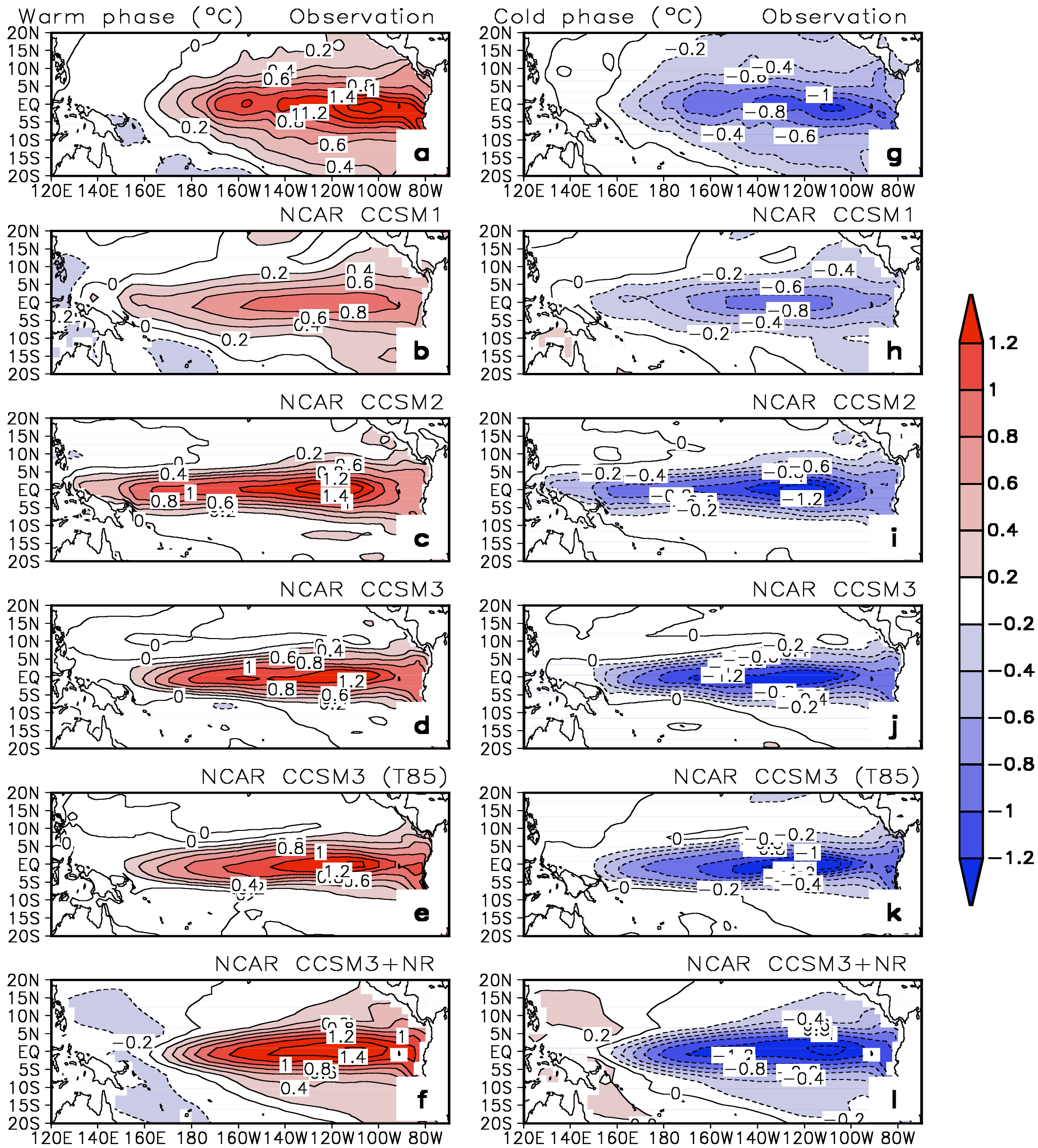

Figure 2. Spatial distributions of composite SST anomalies during El Niño (left panel) and La Niña (right panel) events from observations and five NCAR coupled models. The positive (negative) anomalies of Niño-3 SST with a value greater than 0.5°C (-0.5°C) are selected to construct composites of warm (cold) events. The length of data used in the calculation is 50 years for all the NCAR models and observations (1950–99).

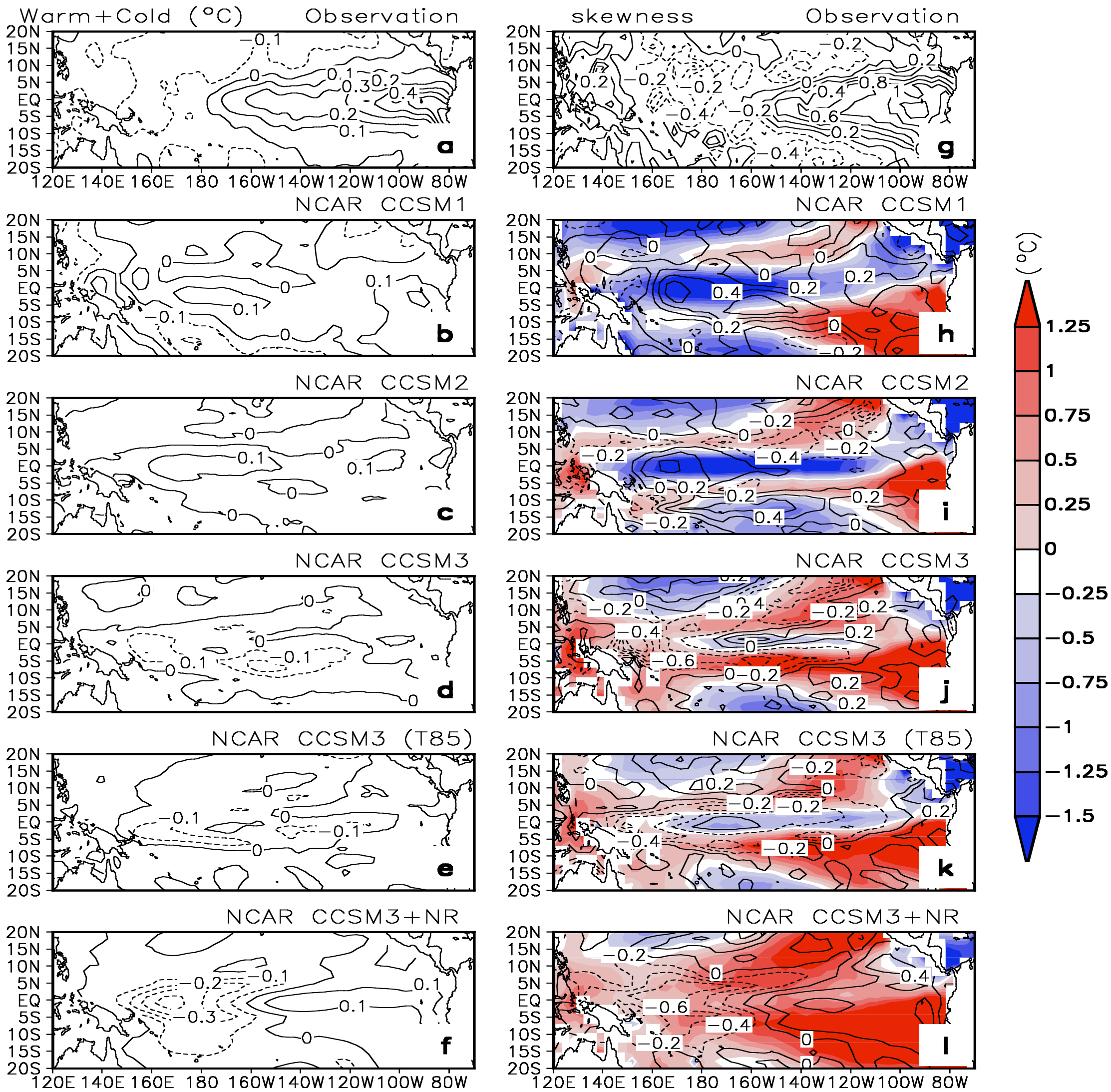

Figure 3. Spatial distributions of the asymmetry between El Niño and La Niña events from observations and five NCAR coupled models. The left panel is the sum of of El Niño and La Niña composites, and the right panel is the skewness pattern of SST anomalies (contour) overlaid with the difference in SST climatology between models and observations (shaded). The positive (negative) anomalies of Niño-3 SST with a value greater than 0.5^{o}C (-0.5^{o}C) are selected to construct composites of warm (cold) events. The length of data used in the calculation is 50 years for all the models and observations (1950–99).

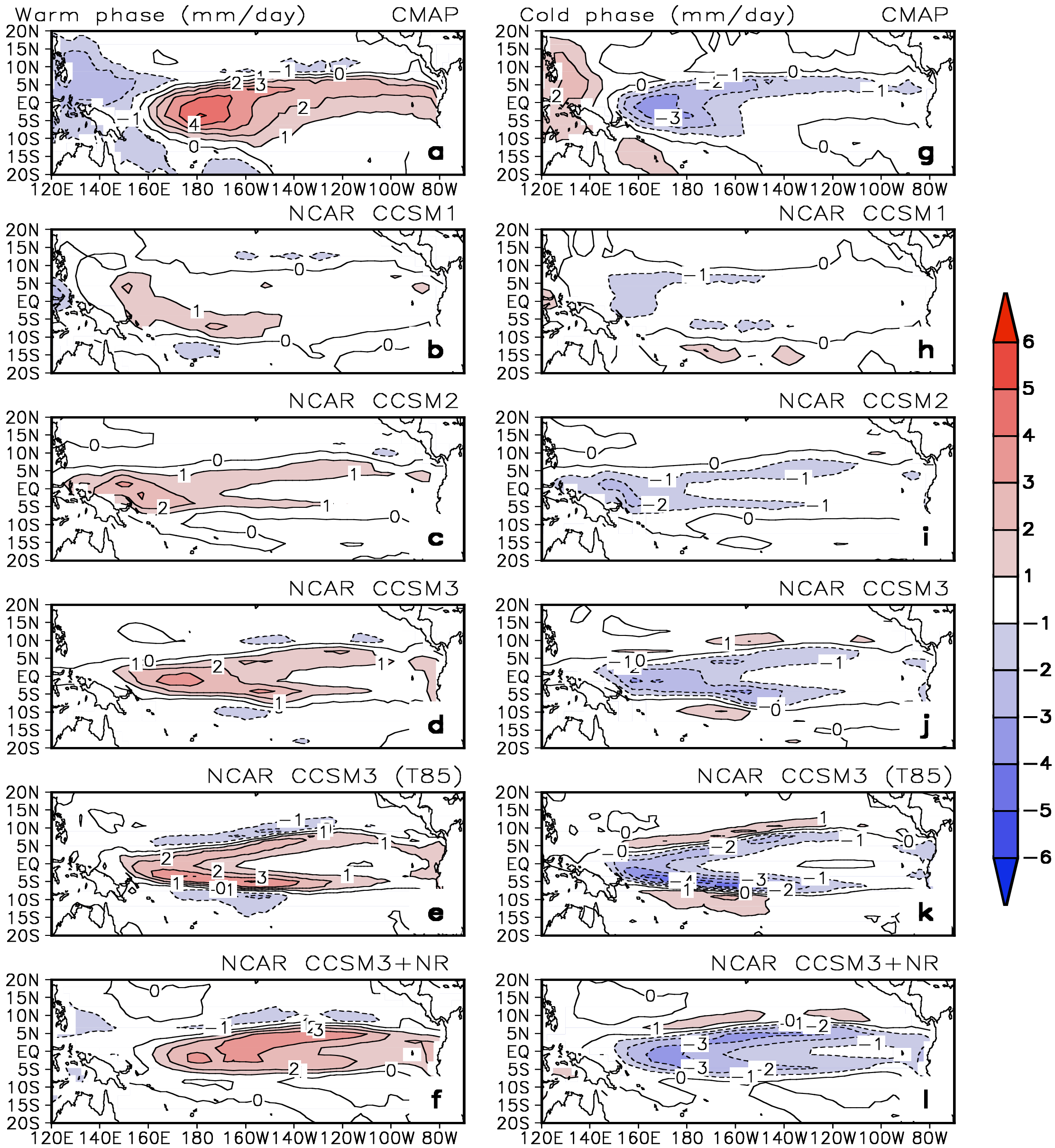

Figure 4. Spatial distributions of precipitation anomalies during warm periods (left panel) and cold periods (right panel). The length of data used in the calculation is 50 years for all the NCAR models and 28 years for the CMAP precipitation (1979-2006).

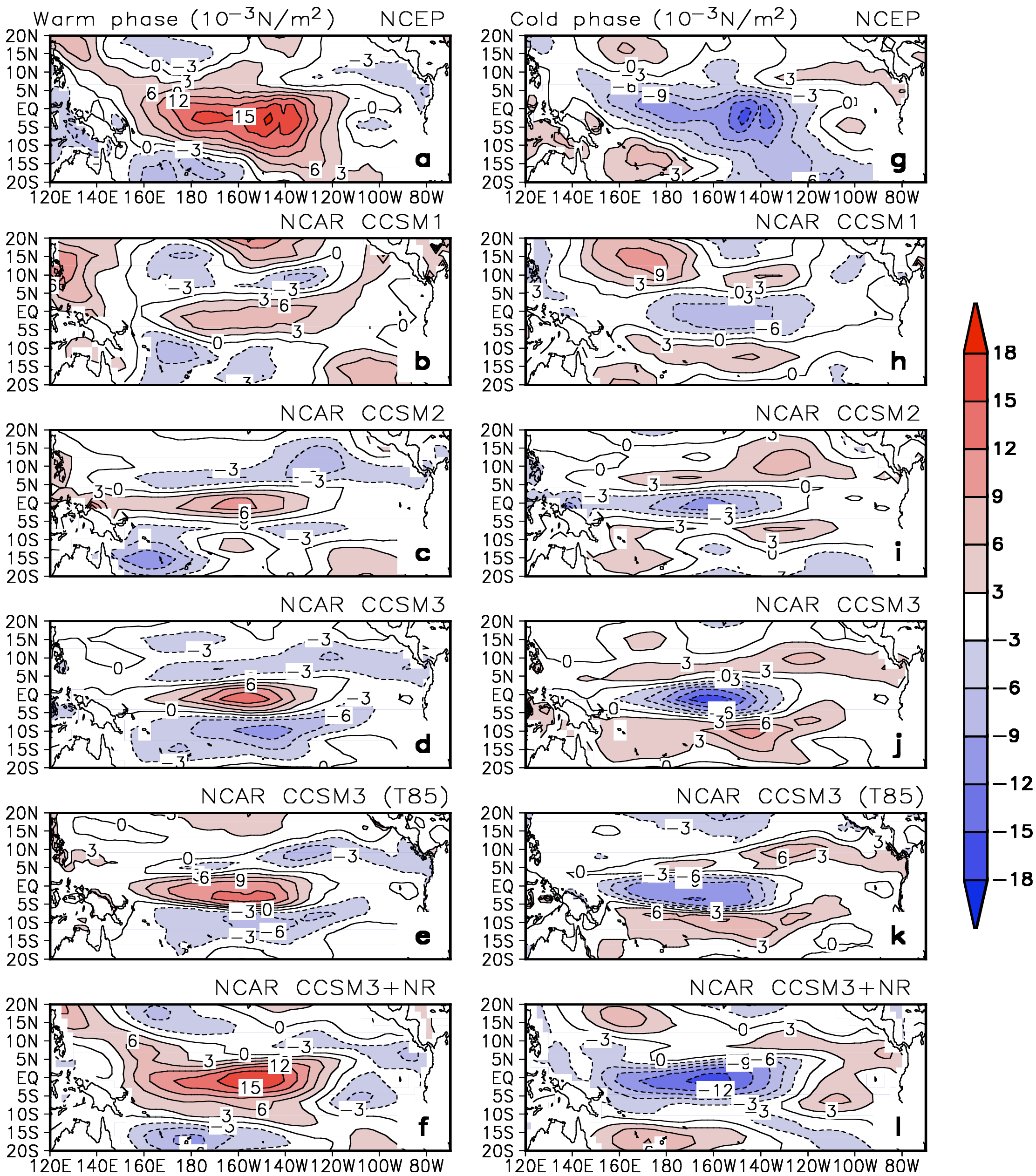

Figure 5. Spatial distributions of zonal wind stress anomalies during warm periods (left panel) and cold periods (right panel). The length of data used in the calculation is 50 years for all the NCAR models and NCEP zonal wind stress (1950-1999).

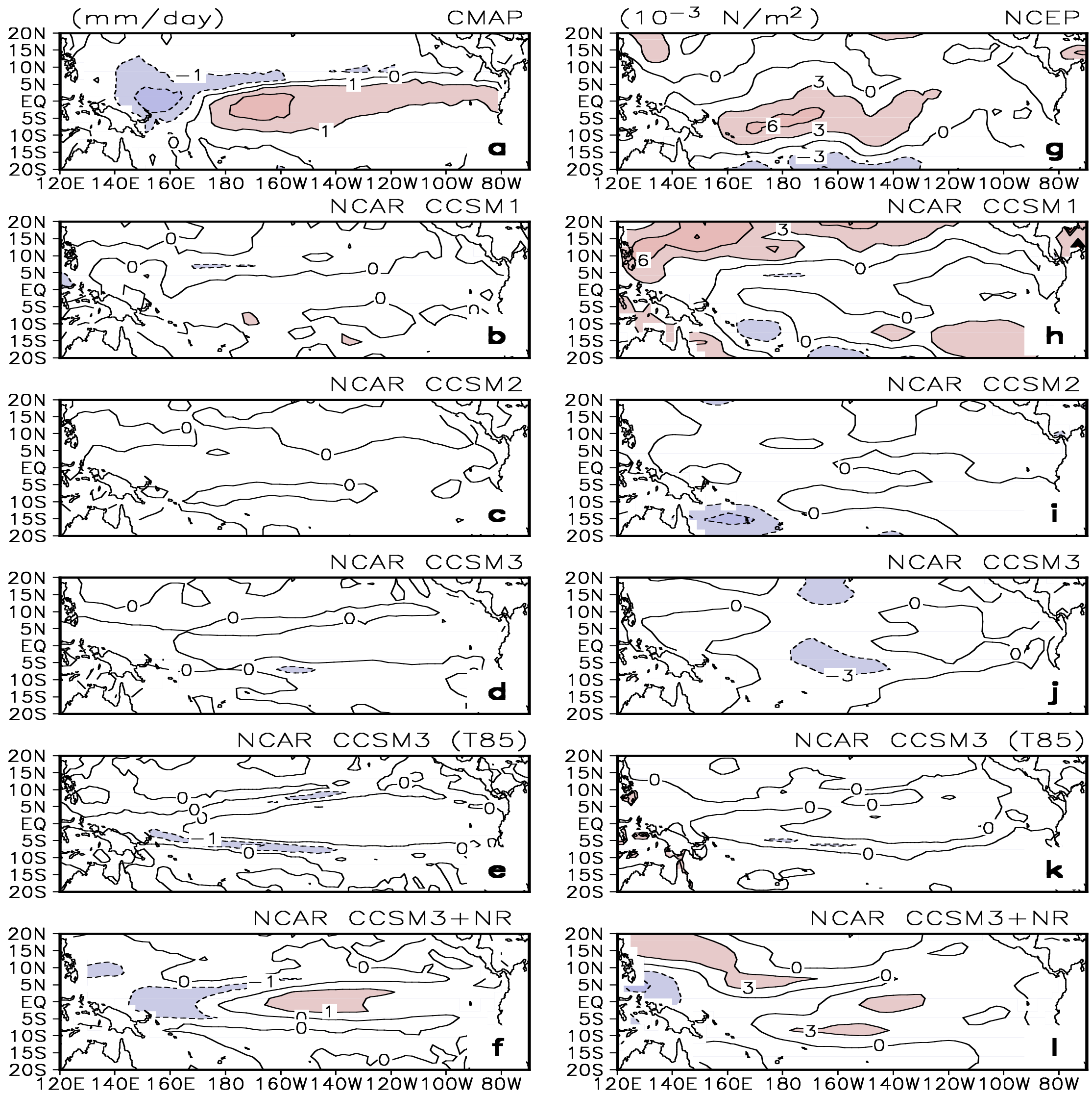

Figure 6. Spatial distributions of asymmetry in precipitation (left panel) and in zonal wind stress (right panel). Shown are the results from the sum between warm anomalies and cold anomalies. The length of data used in the calculation is 50 years for all the models and NCEP zonal wind stress (1950-1999), and 28 years for the CMAP precipitation (1979-2006).

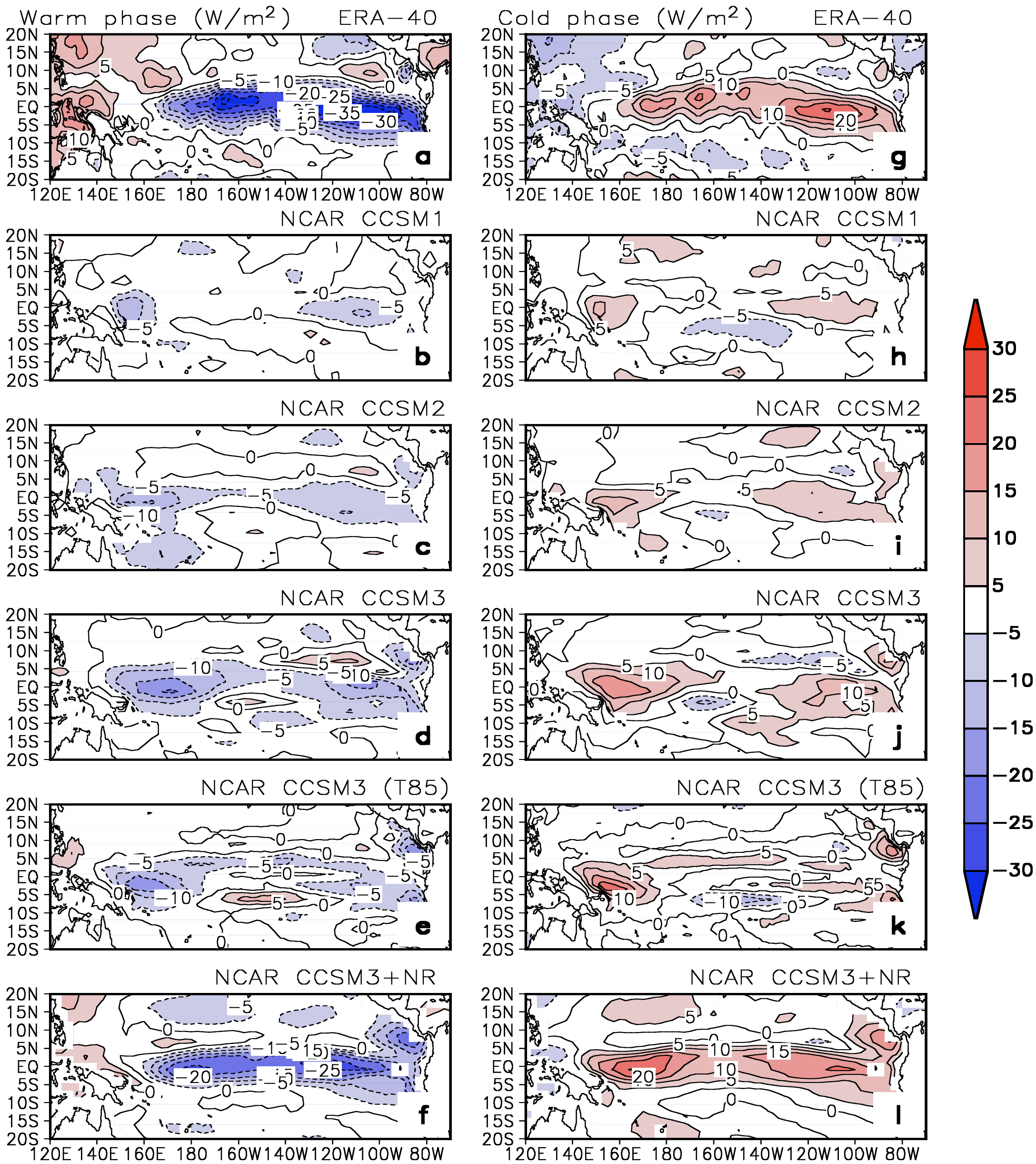

Figure 7. Spatial distributions of net surface heat flux anomalies during warm periods (left panel) and cold periods (right panel). The length of data used in the calculation is 50 years for all the NCAR models and 45 years for the ERA-40 (September 1957-August 2002).

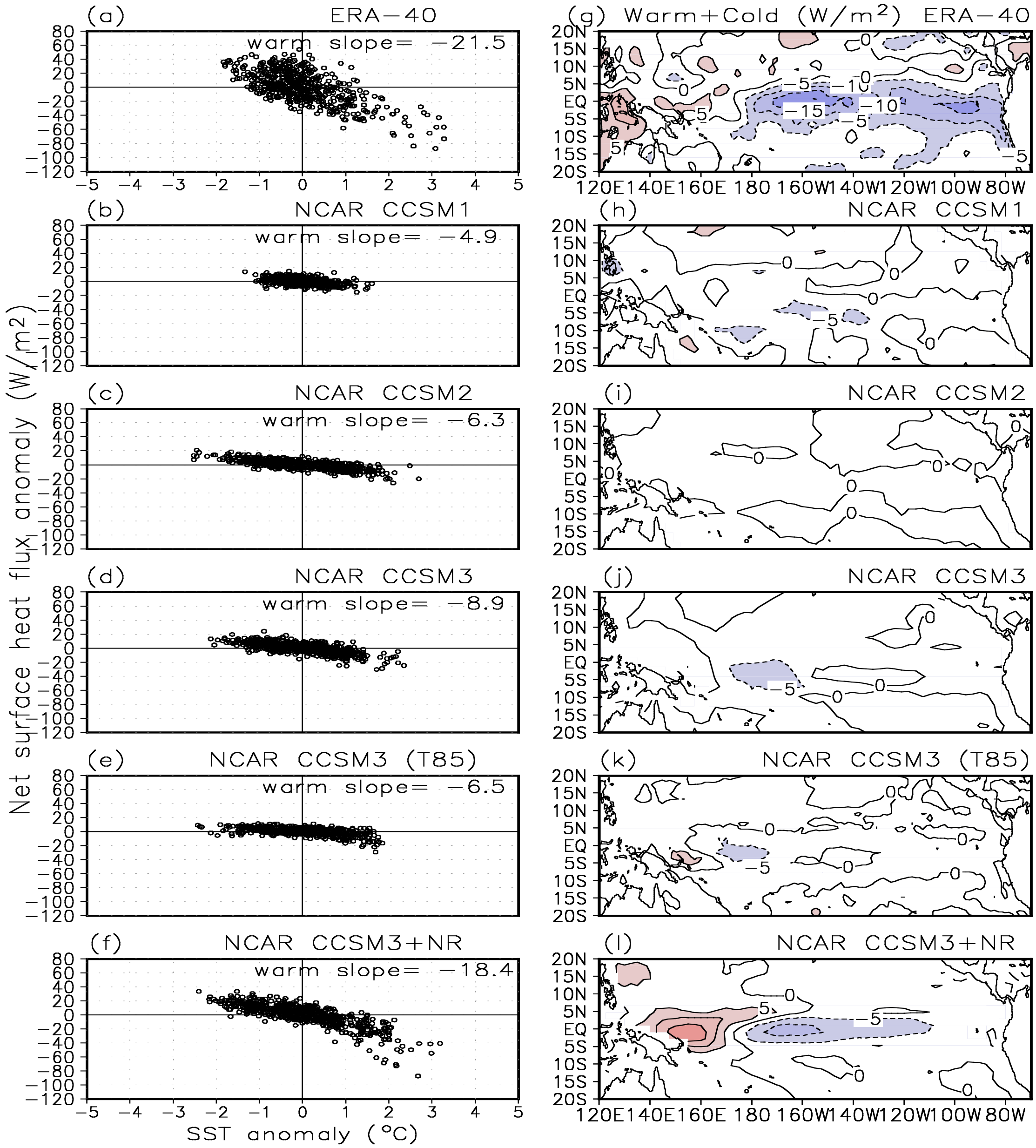

Figure 8. Scatter plot between the net surface heat flux anomalies and the SST anomalies over the Niño-3 region (left panel) and the spatial distributions of asymmetry in net surface heat flux (right panel). The asymmetry in net surface heat flux is defined as the sum between warm anomalies and cold anomalies. The length of data used in the calculation is 50 years for all the models and 45 years for the ERA-40 (September 1957-August 2002).

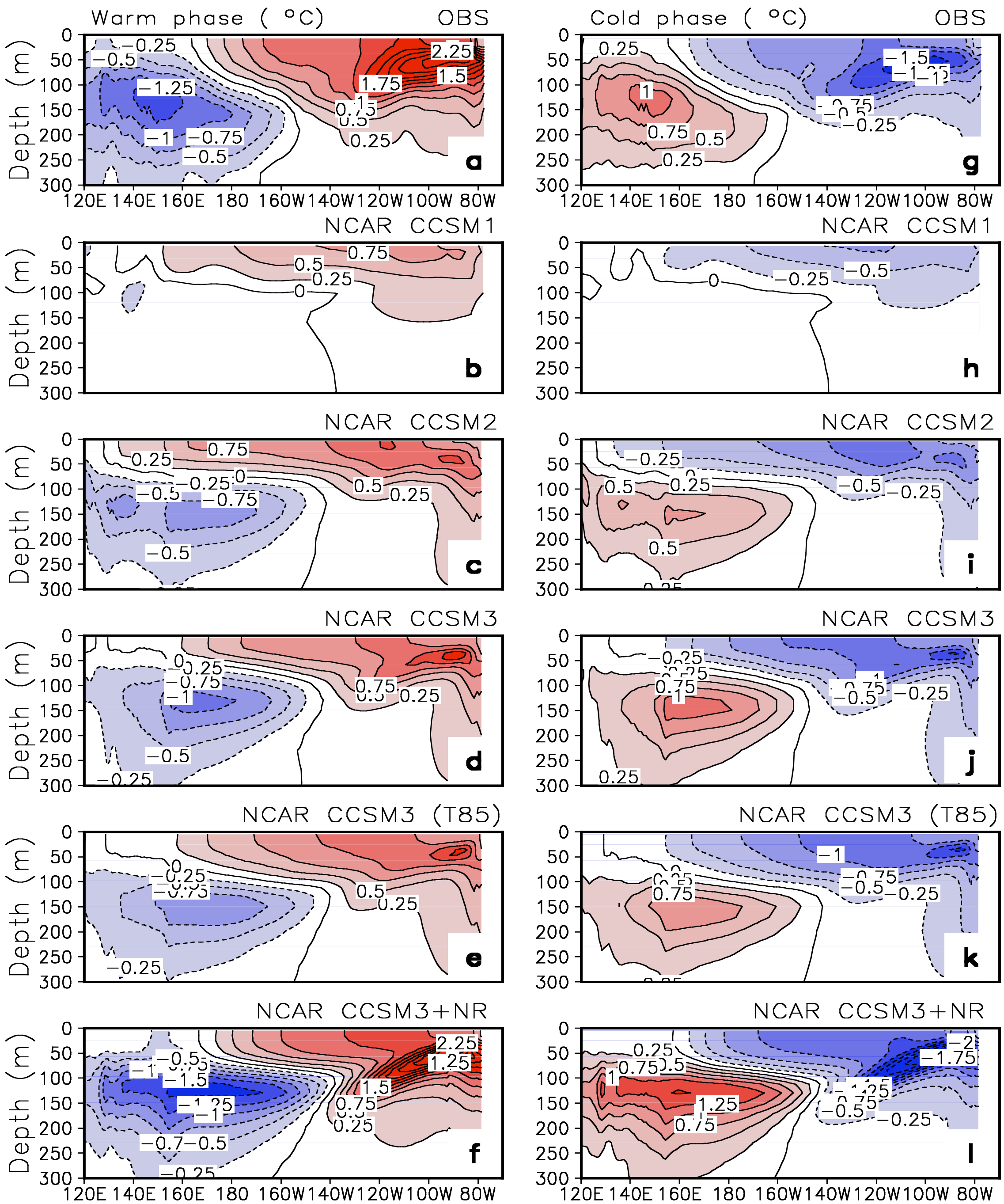

Figure 9. The composite anomalies of equatorial (5°S-5°N) upper ocean temperature during warm periods (left panel) and cold periods (right panel). The length of data used in the calculation is 50 years for all the five models and SODA data (1950–99).

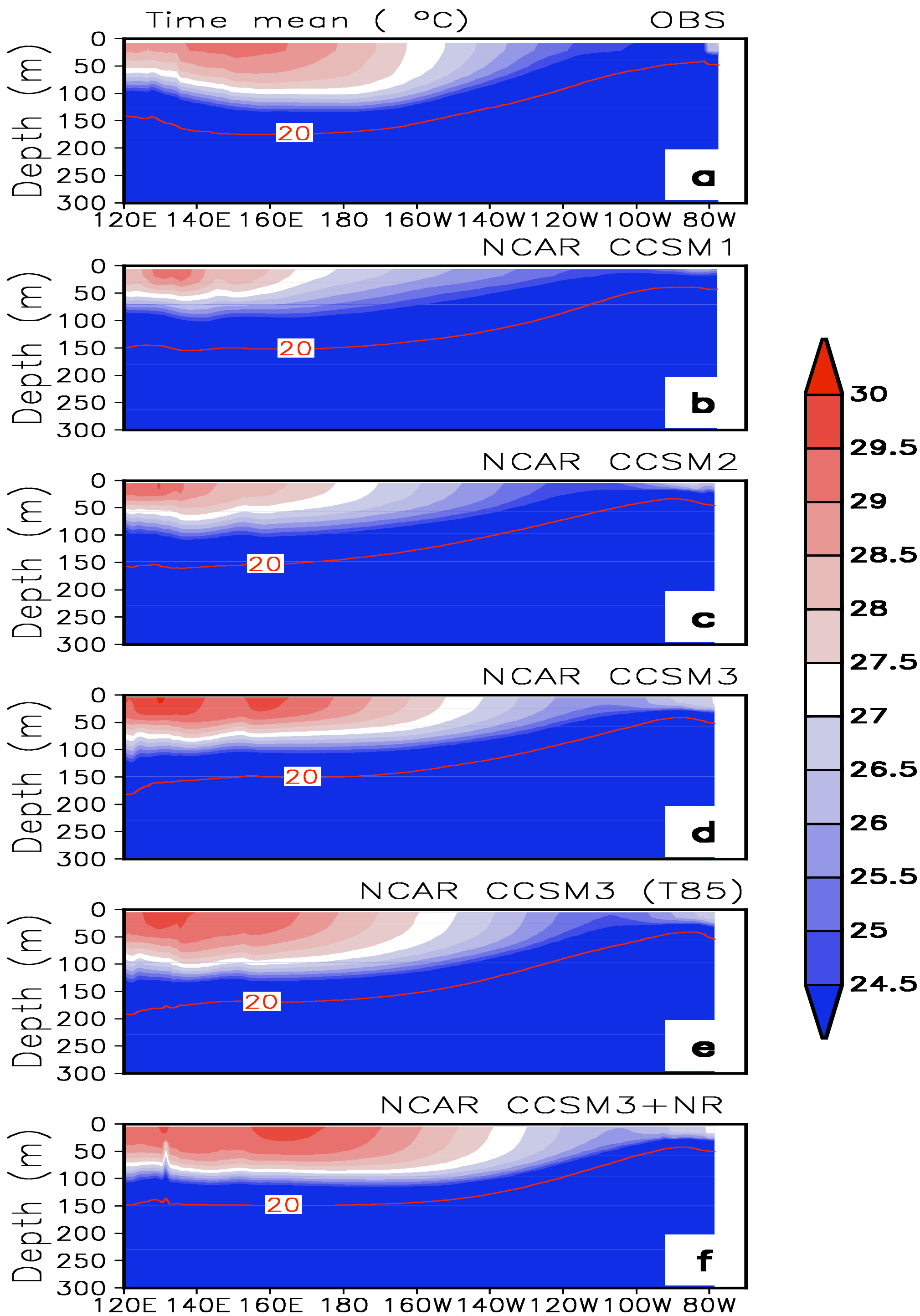

Figure 10. Time-mean equatorial (5°S-5°N) upper ocean temperature from five models and SODA data. The 20 °C isotherm is plotted as red solid line in the figure. The length of data used in the calculation is 50 years for all the five models and SODA data (1950–99).

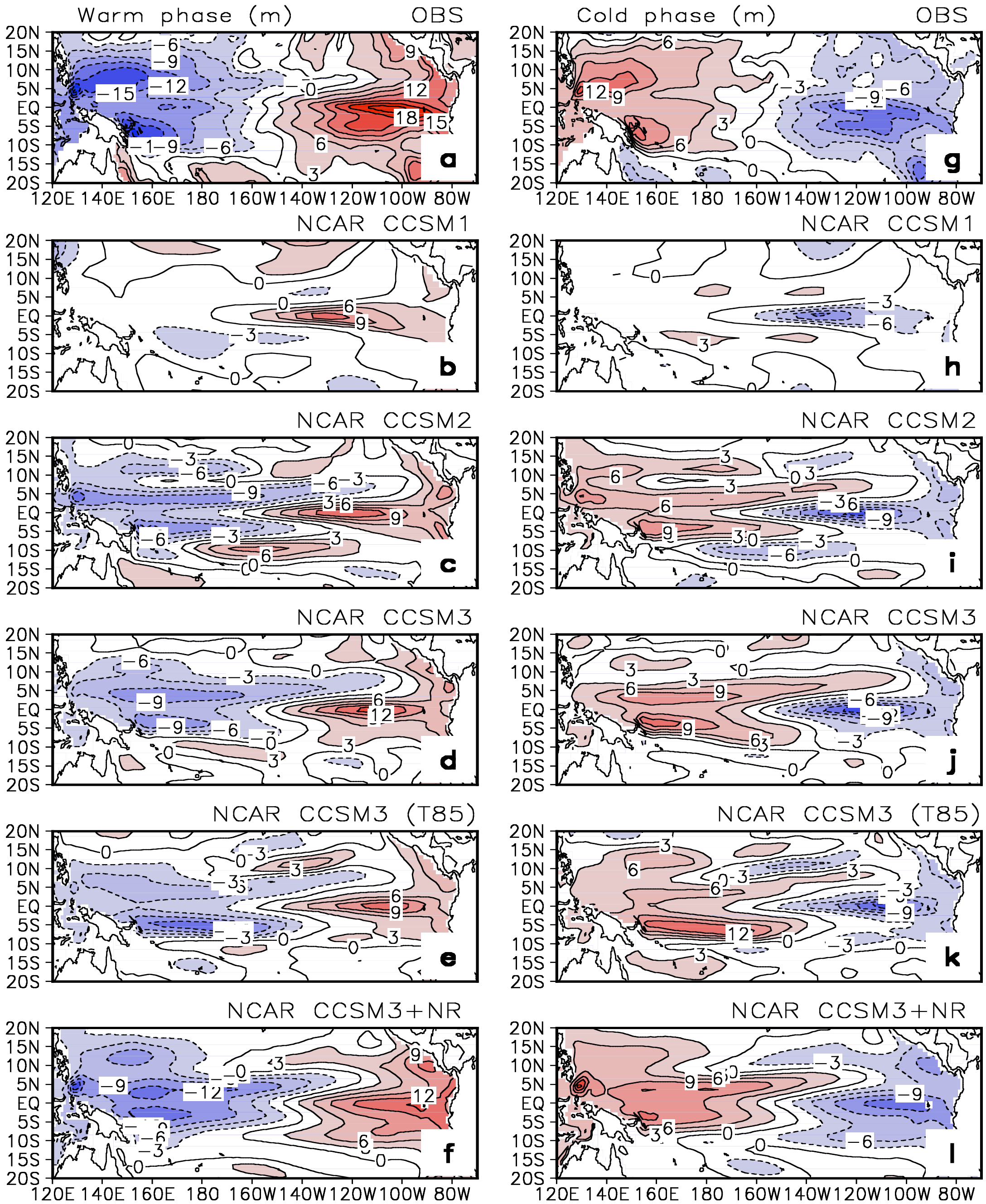

Figure 11. Spatial distributions of 20 ^{o}C isotherm depth anomalies during warm periods (left panel) and cold periods (right panel). The length of data used in the calculation is 50 years for all the five models and SODA data (1950-1999).

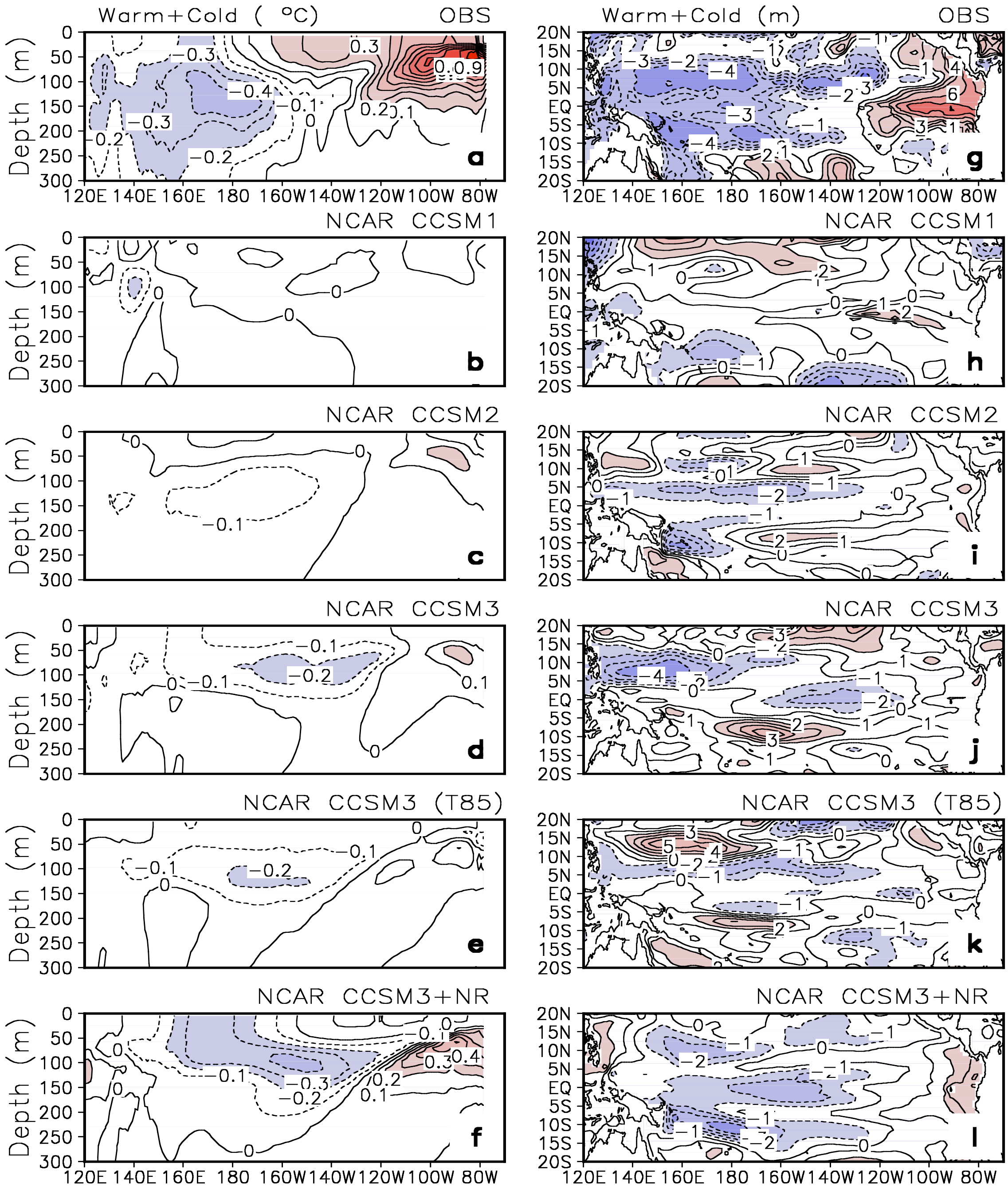

Figure 12. The asymmetry in the equatorial upper ocean temperature (left panel) and in 20 °C isotherm depth (right panel). Shown are the results from the sum between warm anomalies and cold anomalies. The length of data used in the calculation is 50 years for all the five models and SODA data (1950-1999).

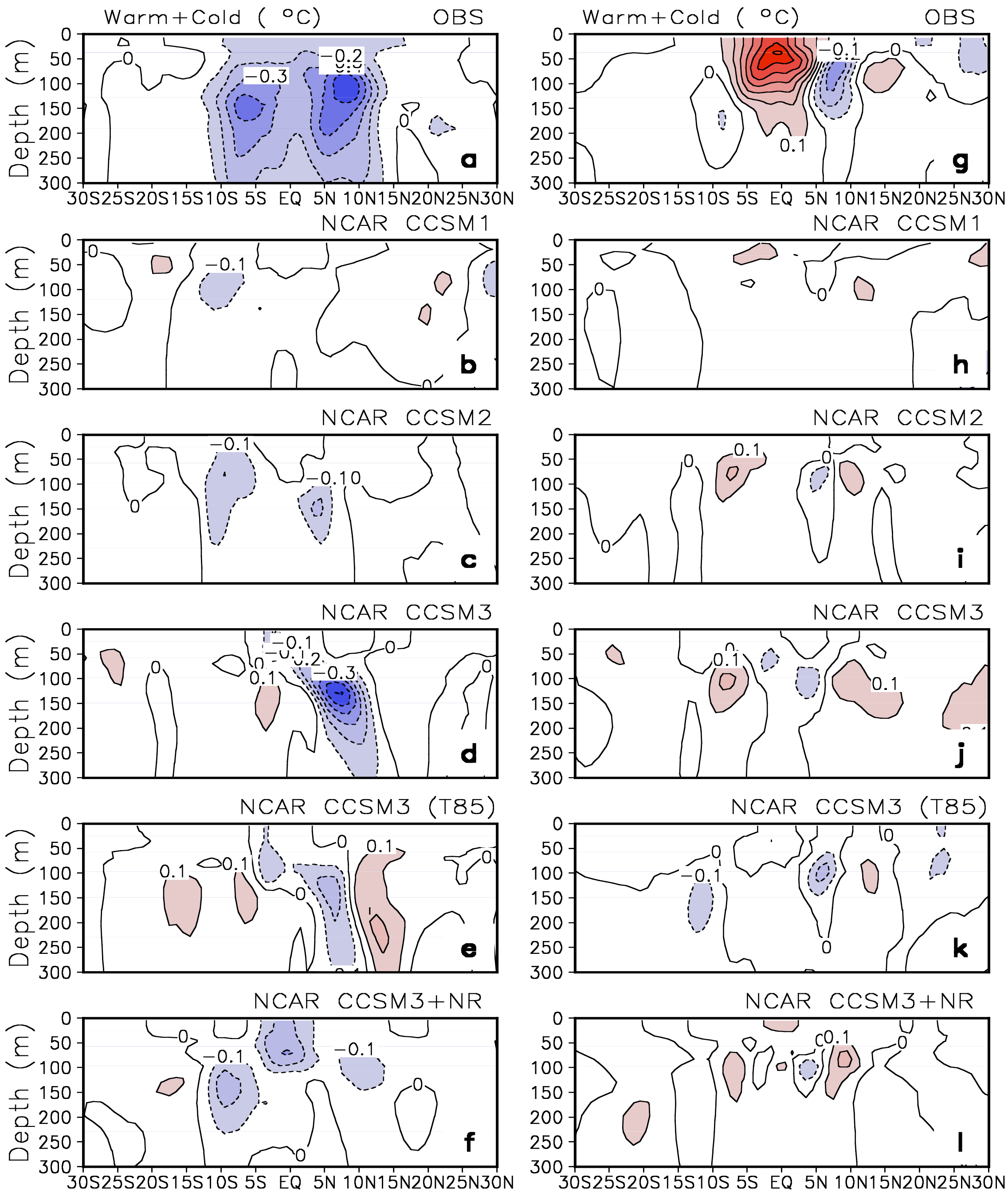

Figure 13. The asymmetry in meridional cross sections of the upper ocean temperature over the western Pacific (130°–170°E) (left panel) and Niño-3 region (210°–270°E) (right panel). Shown are the results from the sum between warm anomalies and cold anomalies. The length of data used in the calculation is 50 years for all the five models and SODA data (1950-1999).

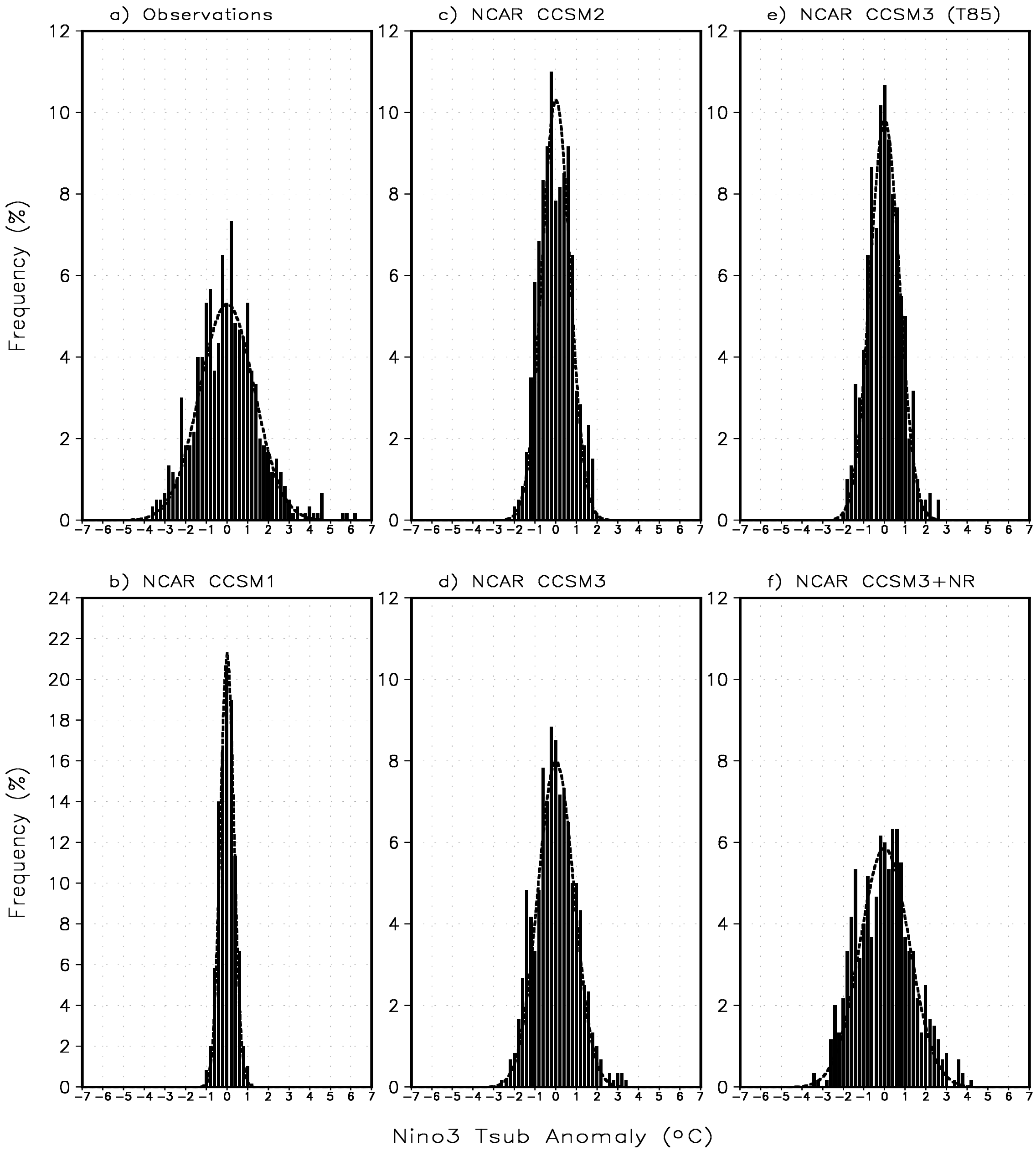

Figure 14. Histograms of the monthly mean Niño-3 subsurface temperature anomalies at 75-m depth. The normal distributions with the respective standard deviation are plotted as dashed line. A bin width of 0.2°C is used. The length of data used in the calculation is 50 years for all the models and SODA data (1950–99).